Editors' Suggestion

Scandium-based point defect in AlN for quantum information processing

Kamil Czelej [1,2,*] Mark E. Turiansky [3] Sai Mu,[4] and Chris G. Van de Walle [3]

[1]*Faculty of Chemical and Process Engineering, Warsaw University of Technology, Ludwika Warynskiego 1, 00-645 Warsaw, Poland*

[2]*Institute of Theoretical Physics, Faculty of Physics, University of Warsaw, Pasteura 5, 02-093 Warsaw, Poland*

[3]*Materials Department, University of California, Santa Barbara, California 93106-5050, USA*

[4]*SmartState Center for Experimental Nanoscale Physics, Department of Physics and Astronomy, University of South Carolina, Columbia, South Carolina 29208, USA*

(Received 9 June 2024; accepted 23 August 2024; published 9 September 2024)

Point defects in wide-band-gap semiconductors have emerged as leading qubit candidates for realizing quantum information processing. Due to the strong spatial localization of the wave functions, these defects can be described as artificial atoms or molecules in a solid-state matrix. Here we propose the positively charged scandium–nitrogen-vacancy defect $(Sc_{Al}V_N)^+$ in AlN as a potential quantum memory, similar to the ST1 center in diamond, based on hybrid density functional theory calculations. $Sc_{Al}V_N$ is stable in the positive charge state over a wide range of Fermi-level positions, where it possesses a singlet ground state and triplet shelving state. By comparing with V_N^+, we elucidate the role of Sc in redshifting the emission energy and enhancing the intersystem crossing via increased spin-orbit coupling. Nuclear spins in the vicinity of $(Sc_{Al}V_N)^+$ may be used as a resource to store the quantum information. We outline an optical spin manipulation protocol for $(Sc_{Al}V_N)^+$ and discuss its utility as a solid-state qubit.

DOI: 10.1103/PhysRevB.110.125116

I. INTRODUCTION

Crystal defects and impurities in wide-band-gap semiconductors are being thoroughly investigated as solid-state platforms for quantum information applications [1–3]. Defects in diamond [4–6] have already been demonstrated to have great utility in quantum technology. Amongst them, the NV [7,8] and SiV [9,10] centers have attracted considerable attention as prototype solid-state qubits. Nevertheless, obstacles in growing and controlling diamond has stimulated work in identifying alternative host materials [2,11], for example, III-V nitrides [12–15].

Wurtzite aluminium nitride (w-AlN) is a binary compound semiconductor with similar properties to diamond, in particular, a large band gap (6.19 eV [16]). A combination of high thermal conductivity ($\kappa = 285$ W/m K) and small thermo-optic coefficient ($dn/dT = 2.32 \times 10^{-5} K^{-1}$) enable the long-term operation of AlN devices with high optical and physical stability [17]. AlN is therefore considered a key material for next-generation electronic and photonic devices, in particular, for high-power and high-temperature applications [18,19]. These properties also make w-AlN a promising host for quantum defects. Moreover, the piezoelectric nature of w-AlN [20] opens the possibility of utilizing spin-mechanical coupling to manipulate the defect states [21,22].

Optical signatures of defects in AlN have been investigated by absorption and photoluminescence (PL) spectroscopies [23–27]. The reported defect-related signatures range from infrared to visible (1.4–2.4 eV) [26] and up to the ultraviolet region (3–4 eV) [24]. Single-photon emission from defects in w-AlN has also been reported [28–30].

Efforts to engineer quantum defects in w-AlN [12–14] have largely focused on identifying analogs to the NV center in diamond. Calculations [12,14] showed that a nitrogen vacancy in the negative charge state (V_N^-) has similarities to the NV^- center in diamond [12]: a triplet ($S = 1$) ground state, C_{3v} symmetry, and similar orbital character. However, the negative charge state is stable only in a narrow window of Fermi levels, and the defect is very likely to photoionize during operation based on the proximity of the states to the conduction band. Varley *et al.* [14] and Seo *et al.* [13] attempted to overcome these issues by considering complexes of the vacancy with transition metals. Based on hybrid density functional theory, they proposed the neutral charge state of $Ti_{Al}V_N$, $Zr_{Al}V_N$, and $Hf_{Al}V_N$ as promising candidates. Introducing the transition metal next to V_N pushes the e states down in the band gap, lowering the separation between a_1 and e states, and enhancing the orbital localization.

In this work, we widen our search of possible quantum defects in w-AlN, relaxing the constraint of resemblance to the NV center in diamond. Removing two electrons from V_N^- results in the positive charge state, which is stable over a wide range of Fermi-level positions. V_N^+ shares characteristics with the ST1 center in diamond [31,32], which unlike the NV center, has a singlet ground state and metastable triplet state. The spin-polarization cycle of such a defect has two major advantages over the NV center in diamond. The first is a significantly longer coherence time, as an electron spin is transferred to a nuclear spin. The second is a large optically detected magnetic resonance (ODMR) readout contrast. Recent experimental investigations demonstrated that the ST1 center enables spin coherent control at room temperature with even larger readout contrast than the NV center [33]. The remarkably high spin contrast makes it promising for use as

*Contact author: kamil.czelej@pw.edu.pl

a quantum memory. V_N^+ in AlN is thus an attractive candidate, but the isolated defect still suffers from needing a very high excitation energy, and having states close to the conduction band. In the same vein as previous efforts we therefore consider a complex with a transition-metal impurity.

Scandium is an attractive candidate because over the last 15 years significant expertise has been acquired on incorporating Sc into AlN. $Al_{1-x}Sc_xN$ alloys were found to exhibit enhanced piezoelectricity compared to AlN [34], and they were also discovered to be ferroelectric [35]; these properties have opened up applications as radio-frequency filters, in high-electron-mobility transistors, and in memory devices.

Using hybrid density functional theory (DFT), we propose $(Sc_{Al}V_N)^+$ as a promising quantum defect in w-AlN. We characterize the formation, stability, and magneto-optical properties of this complex. The positive charge state is stable over a wide range of Fermi-level positions, and the formation energy is low, making it likely to be incorporated. We find that $(Sc_{Al}V_N)^+$ has a singlet $^1A_1$ ground and ^1E excited states, separated by an energy of 3.0 eV. A metastable triplet ^3E state is 0.39 eV below the ^1E excited state, enabling an efficient intersystem crossing and therefore spin-dependent optical manipulation. By quantitatively evaluating the spin-orbit coupling strength, we elucidate the effect of Sc in facilitating the intersystem crossing. We also investigate the zero-field splitting (ZFS), hyperfine parameters in the ^3E state, and the luminescence line shape. Finally, we propose an optical polarization protocol to demonstrate the utility of $Sc_{Al}V_N$ in AlN as a quantum memory.

II. THEORY AND COMPUTATIONAL DETAILS

A. Electronic structure calculations

Our electronic structure calculations are performed using DFT and the projector augmented wave (PAW) method [36,37], as implemented in the Vienna *ab initio* simulation package (VASP) [37,38]. Al $3s^23p^1$, N $2s^22p^3$, and Sc $4s^23d^1$ are treated as valence electrons. An energy cutoff of 450 eV is used for the plane-wave basis set. We apply the screened, range-separated hybrid functional of Heyd, Scuseria, and Ernzerhof (HSE) [39,40] with a mixing parameter $\alpha = 0.32$ and the standard value of the screening parameter $\omega = 0.2$ Å^{-1}. The selected values of α and ω reproduce the 6.19-eV experimental band gap of AlN [16] and result in lattice constants $a = 3.09$ Å and $c = 4.93$ Å, close to the experimental values [41].

To reduce finite-size effects, we use a large $5 \times 5 \times 3$ (300-atom) multiple of the w-AlN primitive cell as a supercell. This approach lets us accurately sample the Brillouin zone with the Γ point only, enabling inspection of Kohn-Sham (KS) wave functions with correct symmetry and degeneracy. The volume of the supercell is kept fixed, and atoms are allowed to relax until the Hellmann-Feynman forces drop below 0.01 eV/Å. Spin polarization is included.

B. Excited-state electronic structure

To calculate the excited-state energies of the defects, we first applied the constrained-DFT Δ-self-consistent field (ΔSCF) method [42] implemented in the VASP code. This approach allows one to determine the excitation energy, zero phonon line (ZPL), and the relaxation energy upon optical excitation. Given that the generalized KS theory is based on single Slater determinants, care needs to be taken to account for the multideterminant nature of the investigated excited states. This issue can be overcome by combining energies from several single-determinant calculations, as proposed by Ziegler [43] and implemented by von Barth [44] within DFT. The single-Slater-determinant calculations are carried out with constrained DFT (cDFT), and we refer to this approach as multideterminant cDFT or mcDFT for short. This approach has recently been applied to several defects, resulting in good agreement with experiment [45–47].

C. Formation energies and charge-state transition levels

The formation energy (ΔH_f^q) of a point defect in charge state q is defined as [48]

$$\Delta H_f^q(E_F) = E_{tot}^q - E_{tot}(\text{bulk}) - \sum_i n_i\mu_i + q(E_{VBM} + E_F) + \Delta E_{corr}, \quad (1)$$

where the Fermi level E_F is referenced to the valence-band maximum (VBM) of w-AlN, E_{tot}^q is the total energy of the supercell containing the defect, $E_{tot}(\text{bulk})$ is the total energy of the perfect crystal in an equivalent supercell, n_i indicates the number of atoms of type i (either host or impurity atoms) that were added to ($n_i > 0$) or removed from ($n_i < 0$) the supercell to create the defect, and μ_i is the chemical potential of the corresponding atoms (i = Al, N, Sc). For example, the chemical potential μ_N represents the energy of the reservoir with which nitrogen atoms are exchanged, reflecting the experimental conditions. It may vary between N-rich (Al-poor) and N-poor (Al-rich) extremes, with bounds set by the calculated formation enthalpy of AlN, $\Delta H_{AlN} = -3.19$ eV. We set μ_{Sc} equal to the energy of metallic Sc in the hexagonal phase for N-poor (Al-rich) conditions. For N-rich (Al-poor) conditions, μ_{Sc} is limited by the formation of ScN in the rocksalt phase:

$$\Delta\mu_{Sc} + \Delta\mu_N = \Delta H_{ScN}. \quad (2)$$

Our calculations yield $\Delta H_{ScN} = -3.42$ eV. The last term, ΔE_{corr}, denotes the finite-size correction for charged defects [49].

The charge-state transition level $\varepsilon(q_1/q_2)$ is defined as the Fermi-level position below which the defect is stable in the charge state q_1 and above which it is stable in charge state q_2. It is calculated as

$$\varepsilon(q_1/q_2) = \frac{\Delta H_f^{q_1}(E_F = 0) - \Delta H_f^{q_2}(E_F = 0)}{q_2 - q_1}. \quad (3)$$

D. Zero-field splitting parameters

Zero-field splitting (ZFS) parameters of the $(Sc_{Al}V_N)^+$ complex in the triplet state were computed from first principles. The S=1 state of $(Sc_{Al}V_N)^+$ is enforced by constrained occupation and we calculate both the spin-spin [50–53] and spin-orbit coupling (SOC) [54] contributions to the ZFS. The spin-spin contribution is calculated as described in Refs. [50–53] as implemented in VASP. Calculating the SOC

contribution requires mapping the fully relativistic total energies of different spin orientations on the defect to the spin Hamiltonian (see Refs. [51–53,55] for more details). This procedure is similar to the estimation of the single-ion magnetocrystalline anisotropy [56] but for a single spin. The spin Hamiltonian with second-order terms is defined as

$$\begin{aligned}\hat{H}_D =& \vec{s}\hat{D}\vec{s} \\ =& - D_{xx}s_x^2 - D_{yy}s_y^2 - D_{zz}s_z^2 \\ & - D_{xy}(s_x s_y + s_y s_x) - D_{xz}(s_x s_z + s_z s_x) \\ & - D_{yz}(s_y s_z + s_z s_y). \end{aligned} \quad (4)$$

The parameters $D_{\alpha\beta}$ can be computed by the four-state mapping method [52,53]:

$$D_{\alpha\beta} = -\frac{1}{4s^2}\left(E_{\alpha\beta}^{(1)} - E_{\alpha\beta}^{(2)} - E_{\alpha\beta}^{(3)} + E_{\alpha\beta}^{(4)}\right), \quad (5)$$

where $E_{\alpha\beta}$ are full relativistic total energies for different spin orientations (see Supplemental Material of Ref. [53] for more details). We note that constrained DFT is vital here to converge to the S=1 state, which possesses a higher energy than the ground state ($S = 0$). To further constrain the spin orientations along different directions for total-energy calculations, we employ the HSE optimized structure and conduct non-self-consistent relativistic calculations using the PBE functional [57,58]. The diagonalization of the $\hat{D}$ matrix yields a traceless tensor D': Within C_{3v} symmetry, the ZFS tensor has the form

$$D' = \begin{bmatrix} -1/3D & 0 & 0 \\ 0 & -1/3D & 0 \\ 0 & 0 & 2/3D \end{bmatrix},$$

and we report the D value obtained from this procedure.

E. Hyperfine interactions

The hyperfine coupling tensor between the electron spin density $\sigma(\boldsymbol{r})$ associated with the electron spin S, and the nucleus J with nonzero nuclear spin I can be expressed as

$$A_{ij} = \frac{1}{2S}\gamma_J\gamma_e\hbar^2\left[\frac{8\pi}{3}\int \delta(\boldsymbol{r}-\boldsymbol{R_J})\sigma(\boldsymbol{r})d\boldsymbol{r} + W_{ij}(\boldsymbol{R_J})\right], \quad (6)$$

where the first term in the square brackets is the Fermi-contact (isotropic) term and

$$W_{ij}(\boldsymbol{R}) = \int\left(\frac{3(\boldsymbol{r}-\boldsymbol{R})_i(\boldsymbol{r}-\boldsymbol{R})_j}{|\boldsymbol{r}-\boldsymbol{R}|^5} - \frac{\delta_{ij}}{|\boldsymbol{r}-\boldsymbol{R}|^3}\right)\sigma(\boldsymbol{r})d\boldsymbol{r} \quad (7)$$

is the dipole-dipole (anisotropic) contribution. γ_J denotes the nuclear magneton of nucleus J and γ_e the electron Bohr magneton.

We calculate the A_{ij} tensor including the core spin polarization effect in the Fermi-contact term within the frozen-valence approximation, relying on the implementation of Szász *et al.* [59]. For these calculations, the plane-wave energy cutoff was increased to 600 eV, while the atomic positions extracted from structural relaxation with energy cutoff of 450 eV were kept fixed.

F. Vibrational properties

We apply density functional perturbation theory (DFPT) to determine the phonon frequencies and phonon modes of the investigated systems. We use the PBE [57,58] functional, which is computationally more efficient and has been shown to be adequate for obtaining accurate vibrational properties [60]. To calculate the vibrational modes with high precision, we applied a very strict 10^{-4} eV/Å force convergence criterion.

The normal mode analysis is based on the inverse participation ratio approach [61]. The magnitude of the IPR is given by

$$\mathrm{IPR} = \sum_{i=1}^{N}\left(x_i^4 + y_i^4 + z_i^4\right)\left[\sum_{j=1}^{N}\left(x_j^2 + y_j^2 + z_j^2\right)\right]^{-2}, \quad (8)$$

where N is the number of atoms in the supercell, and $\mathbf{u}_i = (x_i, y_i, z_i)$ is the normalized 3N-dimensional vector of the atomic displacements of the corresponding vibrational eigenmode.

G. Vibronic coupling and photoluminescence spectrum

We investigate the PL spectrum of $(\mathrm{Sc_{Al}}V_\mathrm{N})^+$ within the framework introduced by Huang and Rhys [62]. The computational implementation of HR theory was provided by Alkauskas *et al.* and successfully demonstrated for the NV and SiNV centers in diamond [63,64]. Details about the computational implementation of HR theory are given in the Supplemental Material [65] (see also Refs. [66–70] therein).

To compute phonon modes we use a 360-atom supercell, which is a $5 \times 3 \times 3$ multiple of the 8-atom orthorhombic unit cell with $a = 3.09$ Å, $b = 5.36$ Å, and $c = 4.95$ Å.

H. Intersystem crossing rate and λ_z component of SOC

Based on the formulation of the nonradiative recombination formalism implemented by Turiansky *et al.* [71] and successfully applied for transition-metal-related defects in hexagonal BN [72], the ISC rate from ^1E to ^3E can be calculated as [73]

$$\Gamma_{\mathrm{ISC}} = 4\pi\hbar\lambda_z^2\tilde{X}(T), \quad (9)$$

where λ_z is the axial component of SOC, and

$$\tilde{X}(T) = \sum_{m,n} w_n |\langle\chi_{fm}|\chi_{in}\rangle|^2\delta(m\hbar\omega_f - n\hbar\omega_i + \Delta E_{if}) \quad (10)$$

is the overlap function between the phonon spectrum of singlet and triplet as a function of the energy splitting ΔE_{if} between ^1E and ^3E, temperature T, and thermal occupation factor w_n. $\omega_{i/f}$ are the phonon frequencies of the initial (i) ^1E and final (f) ^3E states.

To evaluate λ_z we follow the procedure developed by Thiering *et al.* [74] for the NV^- center in diamond. We apply the noncollinear approach in VASP to compute the SOC strength. The SOC is calculated in the C_{3v} high-symmetry configuration of the triplet ^3E. The C_3 axis of the $\mathrm{Sc_{Al}}V_\mathrm{N}$ defect coincides with the [0001] spin quantization axis. SOC can be treated as a small perturbation to the system; thus, the atomic coordinates from the spin-polarized HSE relaxed

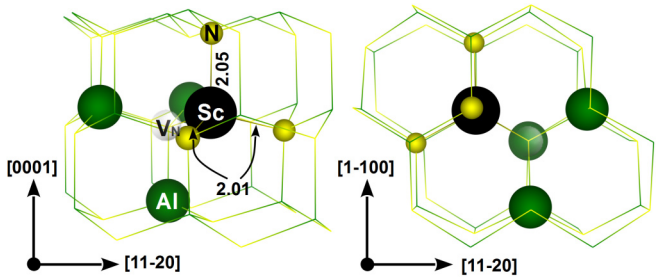

FIG. 1. Ground-state structure of the $(Sc_{Al}V_N)^+$ center. The Sc–N bond lengths are given in Å. Sc, Al, and N are represented by black, green, and yellow spheres, respectively.

geometry are kept frozen. Since the z component of SOC is a diagonal matrix element in the SOC Hamiltonian, we can directly extract the magnitude of the matrix element from the splitting of Kohn-Sham states. In C_{3v} symmetry, the e states are degenerate in the absence of SOC. Once the SOC is switched on, the e states split into e_x and e_y. The ΔSCF procedure enables us to manually set the occupation of one electron either on the e_x or on the e_y state and perform a noncollinear calculation. The total energy difference is the magnitude of λ_z.

III. RESULTS AND DISCUSSION

A. Formation and stability of the $Sc_{Al}V_N$ center

In the wurtzite crystal, there are two types of inequivalent Al–N bonds. The bond parallel to the c axis is slightly elongated compared to the three others, which by symmetry have the same length. There are therefore two symmetry-inequivalent ways to form a complex between V_N and Sc_{Al}. When Sc replaces the Al atom neighboring the vacancy along the c axis, the complex has C_{3v} symmetry. Alternatively, when replacing one of the other three Al atoms, the complex has C_{1h} symmetry. We calculate the formation energy for both cases and find the complex with C_{1h} symmetry to be more stable by 0.24 eV. We therefore focus on the C_{1h}-symmetry complex. However, we note that the energy splitting between the e Kohn-Sham states is small, and the character of the wave functions is still close to C_{3v} symmetry, and therefore it is a good approximation to assume C_{3v} symmetry in the analysis. The relaxed ground-state geometry of the $(Sc_{Al}V_N)^+$ center is shown in Fig. 1. The Sc–N bonds are elongated to 2.01 and 2.05 Å, compared with Al–N bulk values of 1.87 and 1.98 Å.

We first calculate defect formation energies H_f^q as a function of Fermi level to analyze the relative stability of V_N, Sc_{Al}, and $Sc_{Al}V_N$ in various charge states. The results are shown in Fig. 2. Processing in close proximity to equilibrium, such as high-temperature growth or annealing, will result in incorporation of point defects only if they have sufficiently low formation energy. We therefore focus on the most favorable growth conditions for the center, corresponding to the Al-rich limit, which favors formation of both V_N and Sc_{Al}. In the N-rich limit the formation energies of the $Sc_{Al}V_N$ complex and its constituents are significantly higher. This can be attributed to our assumption of equilibrium with ScN as the solubility-limiting phase (which determines the maximum concentration of the impurity). Under N-rich conditions the formation of rocksalt phase ScN sets an upper limit on μ_{Sc} that is significantly lower than the value under N-poor (Al-rich) conditions, rendering the formation energy of Sc_{Al} and the $Sc_{Al}V_N$ complex significantly higher under N-rich conditions. The formation of $Sc_{Al}V_N$ may compete with the formation of intrinsic defects such as V_{Al} or $V_{Al}V_N$. Formation energies for these defects are included in Fig. S1 of the Supplemental Material [65]. Again, Al-rich conditions are favorable for suppressing these defects. A plausible formation mechanism of $Sc_{Al}V_N$ consists of trapping a mobile V_N by Sc_{Al}. First-principles calculations of the V_N migration barrier E_b in AlN and $Al_{1-x}Sc_xN$ yield values ranging from 2.20 to 2.71 eV [75,76]. According to transition-state theory and the methodology demonstrated in Ref. [77], the hopping rate can be calculated as

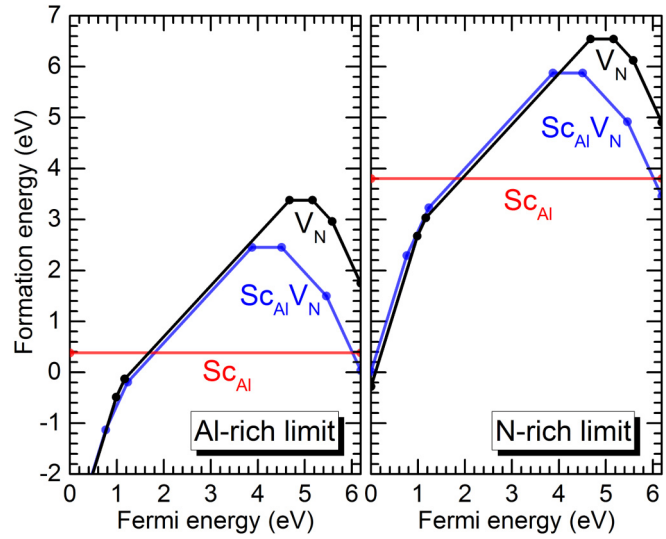

FIG. 2. Formation energy of V_N, Sc_{Al}, and $Sc_{Al}V_N$ as a function of Fermi level for Al-rich (N-poor) and Al-poor (N-rich) conditions.

$$\Gamma = \Gamma_0 \exp\left(\frac{E_b}{k_B T}\right), \tag{11}$$

where Γ_0 is a typical vibrational frequency, T the temperature, and k_B the Boltzmann constant. The estimated temperature at which V_N becomes mobile (corresponding to a hopping rate of 1 s^{-1}) is 580 °C−780 °C.

The results for V_N are in good agreement with prior HSE calculations [12,14,78]; this defect can occur in the 3+, 2+, 1+, 0, 1−, and 2− charge states As expected for a trivalent substitutional impurity, Sc_{Al} is electrically inactive.

Figure 2 shows that $Sc_{Al}V_N$ can be stable in charge states ranging from 3+ to 2−, i.e., its electrical behavior tracks that of V_N. The charge-state transitions (referenced to the VBM) occur at 0.76 eV for (3 + /2+), 1.22 eV for (2 + /+), 3.87 eV for (+/0), 4.50 eV (1.69 eV below the CBM) for (0/−), and 5.46 eV (0.73 eV below the CBM) for (−/2−). The positive charge state of $Sc_{Al}V_N$ is stable over a wide range of Fermi energies, and the corresponding formation energy is modest (even when conditions are not in the Al-rich limit), ensuring that it can be incorporated.

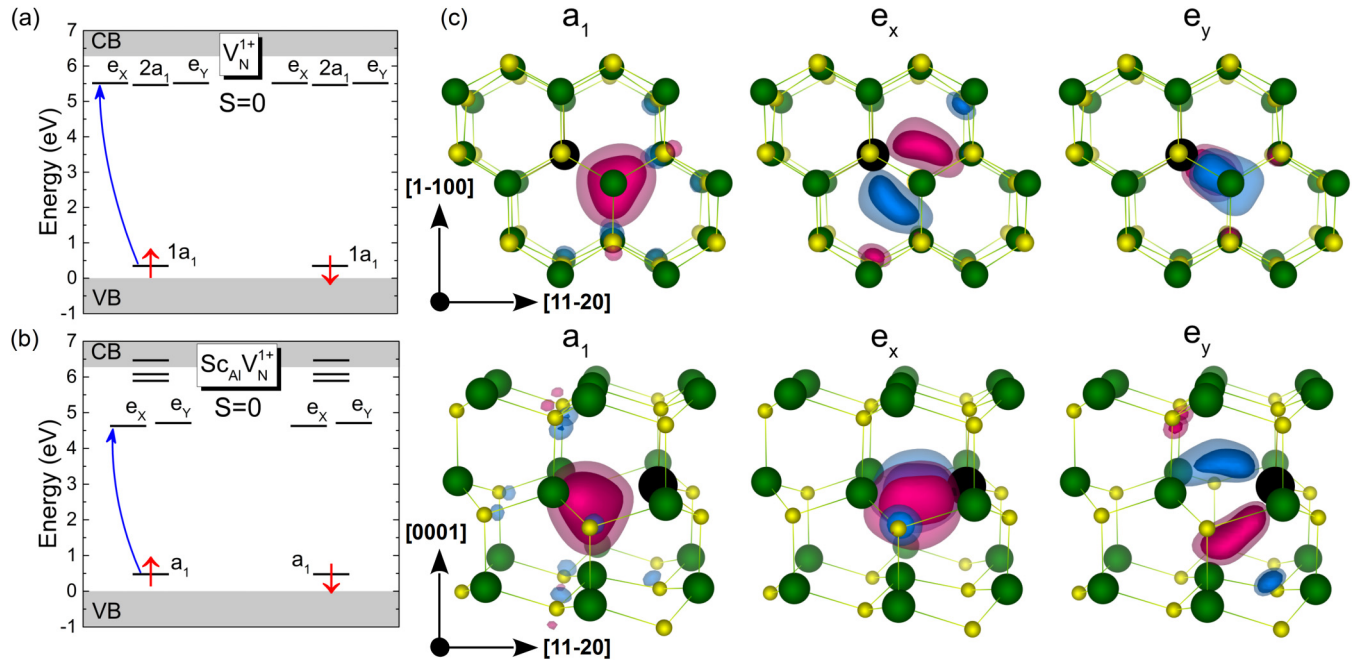

FIG. 3. HSE Kohn-Sham eigenvalue spectra of (a) V_N^{1+} and (b) $(Sc_{Al}V_N)^+$ defects in AlN. The gray shaded areas represent valence and conduction bands. Spin-up and -down channels are depicted and the occupied levels are represented by red arrows. Localized defect-related states in the band gap are labeled with their symmetry representation. (c) Isosurfaces of the spin-up Kohn-Sham wave functions for the $(Sc_{Al}V_N)^+$ complex. The top and bottom rows represent the same wave functions of the complex viewed from two different, mutually orthogonal crystallographic directions. The red (blue) lobes indicate the positive (negative) phase of the wave functions. Sc, Al, and N are represented by black, green, and yellow spheres, respectively.

To stabilize the desired positive charge state, the Fermi level needs to be between 1.22 eV and 3.87 V. We propose that controlling the Fermi level can be accomplished by doping with carbon, which acts as a deep acceptor in AlN when incorporated on the nitrogen site (which is indeed most favorable under the Al-rich conditions we assume here). Assuming that some unintentional donors are present (such as oxygen, which is usually unavoidable), and that otherwise carbon is the dominant impurity, charge neutrality would pin the Fermi level at the $(0/-)$ transition level of carbon (see Fig. S1 in the Supplemental Material [65]). First-principles calculations [79] placed this level at 1.88 eV above the VBM, ensuring that V_N and $Sc_{Al}V_N$ would be in the positive charge state.

To assess the tendency for complex formation, we compute the binding energy of the $Sc_{Al}V_N$ complex referenced to isolated Sc_{Al} and V_N constituents. Focusing on the positive charge state of the complex, the binding energy is defined as

$$E_b = \Delta H_f\left(Sc_{Al}^0\right) + \Delta H_f(V_N^+) - \Delta H_f[(Sc_{Al}V_N)^+]. \quad (12)$$

Using this definition, we find a value of 0.51 eV, a positive value indicating that the complex is stable.

B. Electronic structure of $(Sc_{Al}V_N)^+$

We proceed to analyze the quantum behavior, optical properties, and magnetic characteristics of the $Sc_{Al}V_N$ center. We focus on the positive charge state, which is stable over the largest range of Fermi levels; we will see that the electronic configuration of this charge state satisfies fundamental requirements to be used as a quantum-memory-like qubit. We calculate the Kohn-Sham eigenvalue spectrum and scrutinize defect-induced gap states by means of group theory.

We first consider the electronic structure of V_N^+, as it will shed light on the behavior of the complex. Removing a single N atom results in a relatively high-symmetry defect: in a cubic crystal, the vacancy would have T_d symmetry, but in a wurtzite crystal, we find V_N^+ to have C_{3v} symmetry, as reflected in the Kohn-Sham states shown in Fig. 3(a). The occupied states in the gap transform like the a_1 irreducible representation of C_{3v}. Three unoccupied states are present high in the gap; they would transform like t_2 states in T_d symmetry, but split into two e states and one a_1 state (labeled $2a_1$) in the wurtzite crystal. We find this crystal-field splitting to be very small, $\sim$60 meV, indicating relatively high symmetry for V_N^+.

In our calculations, Sc_{Al} does not introduce any defect-related states into the gap and is present only in the neutral charge state. As a consequence, it does not alter the magnetic and optical properties of the AlN crystal. However, the presence of Sc_{Al} has important consequences for the complex.

Figure 3(b) shows the Kohn-Sham states of $(Sc_{Al}V_N)^+$. Notable differences compared to V_N^+ are seen in the unoccupied defect states. Sc_{Al} introduces larger symmetry-breaking distortions in the structure compared to V_N^+, leading to a much larger splitting of the unoccupied states. The lowest unoccupied orbitals are e orbitals. We visualize the real-space a_1, e_x, and e_y wave functions in Fig. 3(c). To enable better inspection of the symmetry and localization of the orbitals, we also provide three GIF files representing a 90° rotation around the [0001] axis for each wave function (see Supplemental Material [65]). The e states in $Sc_{Al}V_N$ have considerable Sc $3d$ character (as determined by the site and orbital

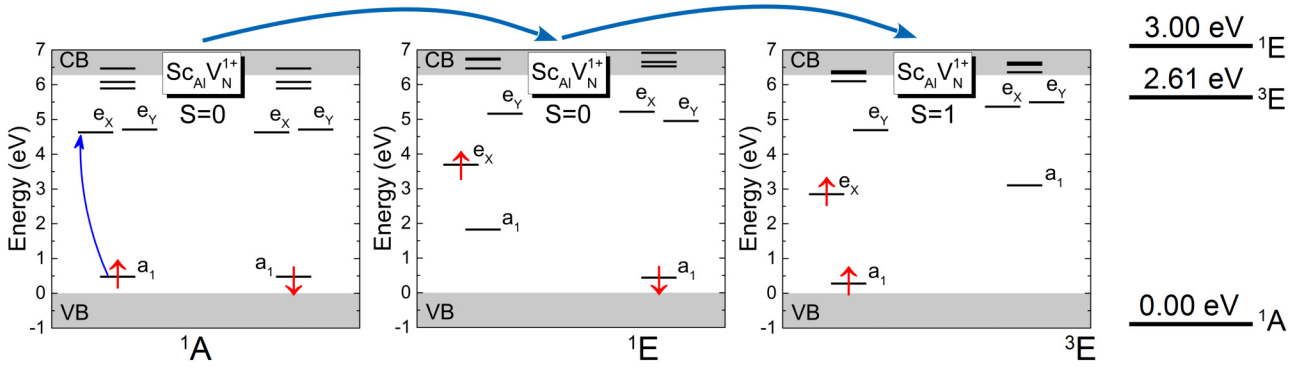

FIG. 4. Defect level diagrams representing the optical spin polarization cycle $Sc_{Al}V_N^{1+}$ together with the energy of the excited states ^1E and ^3E with respect to the ground state ^1A.

projections from the calculation output), whereas in V_N, they were predominantly Al $2p$. Another noticeable difference in the electronic structure is significantly deeper localization of defect states within the fundamental band gap and larger separation from the CB and VB edges.

In the ground state both spin channels of the a_1 state are occupied and the e states are empty, forming a closed-shell $a_1^2e^0$ electron configuration. The multielectron $S = 0$ singlet state can be therefore described by a single Slater determinant as $^1A = |a_1^{\uparrow}a_1^{\downarrow}\rangle$.

The first spin-conserving excited state is a singlet ^1E where one electron is promoted to an e state, forming the $a_1^1e^1$ electron configuration. This state can be expressed as

$$^1E = \frac{1}{\sqrt{2}}\begin{cases}\mathcal{A}(|e_+^{\uparrow}a_1^{\downarrow}\rangle - |e_+^{\downarrow}a_1^{\uparrow}\rangle),\\ \mathcal{A}(|e_-^{\uparrow}a_1^{\downarrow}\rangle - |e_-^{\downarrow}a_1^{\uparrow}\rangle),\end{cases} \tag{13}$$

where $\mathcal{A}|xy\rangle = \frac{1}{\sqrt{2}}(|xy\rangle - |yx\rangle)$ is the usual antisymmetrizing operator, and $e_{+(-)} = e_x + (-)ie_y$. As the doubly degenerate e orbital is occupied by one electron, the system is Jahn-Teller unstable and lowers its symmetry to C_{1h}.

We calculate the ZPL for the transition from the ground state to be 3.00 eV within the ΔSCF method. However, as seen in Eq. (13), the ^1E state combines two Slater determinants; therefore, we also applied the mcDFT approach. The energy expression for the ^1E state reads as

$$E[^1E] = 2E[a_1^{\uparrow}e^{\downarrow}] - E[a_1^{\uparrow}e^{\uparrow}]. \tag{14}$$

We find a ZPL energy of 3.06 eV with the mcDFT approach, very close to the 3.00 eV value calculated with only single determinants. To simplify the analysis, we only use single determinants to calculate the energetics. For V_N^+, we find a value of 4.15 eV, which emphasizes the role of Sc in redshifting the emission energy by lowering the symmetry of the center.

In addition to the singlet ^1E excited state we find a triplet ^3E with an energy 0.39 eV below the singlet; see Fig. 4. The ^1E and ^3E states share the same $a_1^1e^1$ electron occupation and therefore the restoring forces acting on atoms while switching between these states should be small. In fact, our calculations yield a Franck-Condon shift of ∼70 meV, confirming that the geometry of both states is nearly unchanged.

When SOC is introduced, the spin and orbital parts of the wave function must be considered together. Therefore, we apply the double-group notation [80] to further investigate the excited-state electronic structure of $(Sc_{Al}V_N)^+$. For the C_{3v} point group, the double group includes the A_1, A_2, and E irreps, but with additional consideration for spinor (spin-$\frac{1}{2}$) representations. In double-group notation, the ^3E manifold is composed of $E_{x,y}$ ($m_s = 0$), and $A_1 \bigoplus A_2 = A_{1,2}$ and $E_{1,2}$ ($m_s = \pm 1$) spin projections. These three states (see Fig. 5) can be expressed as

$$E_{x,y} = \frac{1}{\sqrt{2}}\begin{cases}\mathcal{A}(|e_+^{\uparrow}a_1^{\downarrow}\rangle + |e_+^{\downarrow}a_1^{\uparrow}\rangle),\\ \mathcal{A}(|e_-^{\uparrow}a_1^{\downarrow}\rangle + |e_-^{\downarrow}a_1^{\uparrow}\rangle),\end{cases} \tag{15}$$

$$A_{1,2} = \begin{cases}\mathcal{A}|e_-^{\uparrow}a_1^{\uparrow}\rangle,\\ \mathcal{A}|e_+^{\downarrow}a_1^{\downarrow}\rangle,\end{cases} \tag{16}$$

$$E_{1,2} = \begin{cases}\mathcal{A}|e_+^{\uparrow}a_1^{\uparrow}\rangle,\\ \mathcal{A}|e_-^{\downarrow}a_1^{\downarrow}\rangle.\end{cases} \tag{17}$$

In Sec. III E we will demonstrate that the $E_{x,y}$ state is especially important as it plays a crucial role in the optical polarization cycle of $Sc_{Al}V_N^{1+}$ center.

Finally, we report the ZFS parameter for the ^3E shelving state. The calculated ZFS D is mainly SOC dominated, with a contribution of 12.96 GHz from spin-orbit interaction and 0.45 GHz from the spin-spin dipolar interaction.

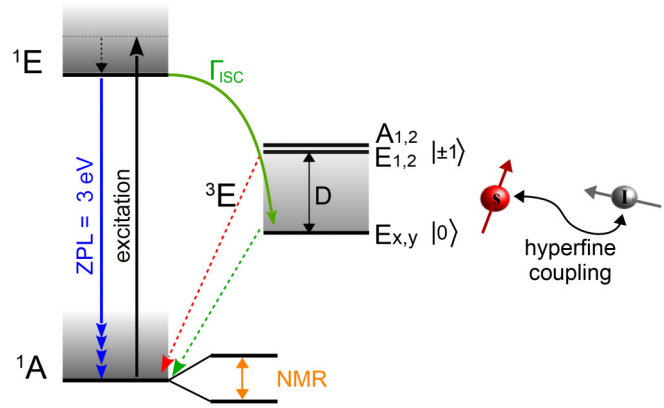

FIG. 5. Schematic illustrating optical control and readout of the nuclear spin mediated by the electronic triplet spin ancilla.

TABLE I. Hyperfine parameters of the V_N^{1+} and $(Sc_{Al}V_N)^+$ centers in the ^3E excited state calculated with the HSE functional. R (MHz) is the magnitude of the hyperfine parameters, and θ (deg), φ (deg) provide the direction in spherical coordinates. The θ value describes the polar angle referenced to the [0001] direction and φ is the azimuthal angle referenced to the $[1\bar{1}00]$ direction [in the (0001) plane]. The last Al atom in the list is the one oriented along the c axis relative to the vacancy.

		A_{xx}			A_{yy}			A_{zz}		
		R	θ	φ	R	θ	φ	R	θ	φ
V_N^{1+}	1 ^{27}Al	86	69°	−137°	56	76°	127°	54	25°	6°
	2 ^{27}Al	205	69°	−32°	154	68°	67°	154	32°	−162°
	3 ^{27}Al	35	69°	76°	15	82°	169°	12	22°	−80°
	4 ^{27}Al	−25	90°	−112°	−23	89°	−22°	−12	1°	138°
$Sc_{Al}V_N^{1+}$	^{45}Sc	147	90°	60°	143	79°	150°	72	11°	−30°
	1 ^{27}Al	145	72°	−83°	101	61°	177°	100	35°	35°
	2 ^{27}Al	145	72°	23°	101	61°	123°	100	35°	−95°
	3 ^{27}Al	−10	87°	−30°	−10	90°	−120°	−4	3°	150°

C. Hyperfine parameters

To aid in experimental identification of the metastable ^3E triplet state of V_N^+ and $(Sc_{Al}V_N)^+$, we compute the hyperfine coupling, which can be probed in experiments such as optically detected magnetic resonance or photoinduced electron paramagnetic resonance. We consider the magnetic isotopes that are most abundant and stable, i.e., ^{27}Al ($I = \frac{5}{2}$; abundance = 100%), ^{14}N ($I = 1$; abundance = 99.6%), and ^{45}Sc ($I = \frac{7}{2}$; abundance = 100%). The calculated hyperfine parameters for Sc and for the nearest-neighbor atoms are listed in Table I. For $(Sc_{Al}V_N)^+$, the values of the hyperfine parameters on Sc and two of the Al neighbors are >100 MHz, while the value on the remaining Al atom is one order of magnitude smaller (<10 MHz) and negative. The calculated hyperfine structure clearly indicates lower symmetry of the ^3E excited state.

D. Electron-phonon coupling and photoluminescence of $Sc_{Al}V_N^{1+}$ center

The simulated PL line shape associated with the spin-conserving $^1E \rightarrow {}^1A$ optical transition is depicted in Fig. 6(a). Our simulation predicts a broad, largely featureless phonon sideband spanning a range of nearly 600 meV below the ZPL. Interestingly, this sideband bears a strong resemblance to the PL sideband of the ST1 center in diamond [32].

The partial Huang-Rhys (HR) factor S_k and the spectral function of electron-phonon coupling $S(\hbar\omega)$ are depicted in Fig. 6(b). Low-energy phonon modes centered at 28 meV and spanning ∼12 meV couple especially strongly to the $^1E \rightarrow {}^1A$ transition. The highest partial HR factor $S_k = 0.21$ is found for a 32-meV delocalized phonon mode (IPR = 0.000 34). This mode alone contributes ∼6% to the total HR factor $S(0) = 3.62$. We find only one clearly visible quasilocal vibrational mode, at 74 meV, that could potentially be identified via infrared spectroscopy. This mode is doubly degenerate of e symmetry, with an IPR = 0.024. It mainly involves a stretching motion of the three Al–N and the Sc–N bonds neighboring the vacancy. The calculated DW factor $w_{ZPL} = 2.7\%$ is very close to $w_{ZPL} = 2.4\%$ for the NV center in diamond [63].

E. Spin-polarization cycle and quantum protocol of $Sc_{Al}V_N^{1+}$ center

Based on the appealing electronic structure and magneto-optical properties of $(Sc_{Al}V_N)^+$ center, we propose an optical

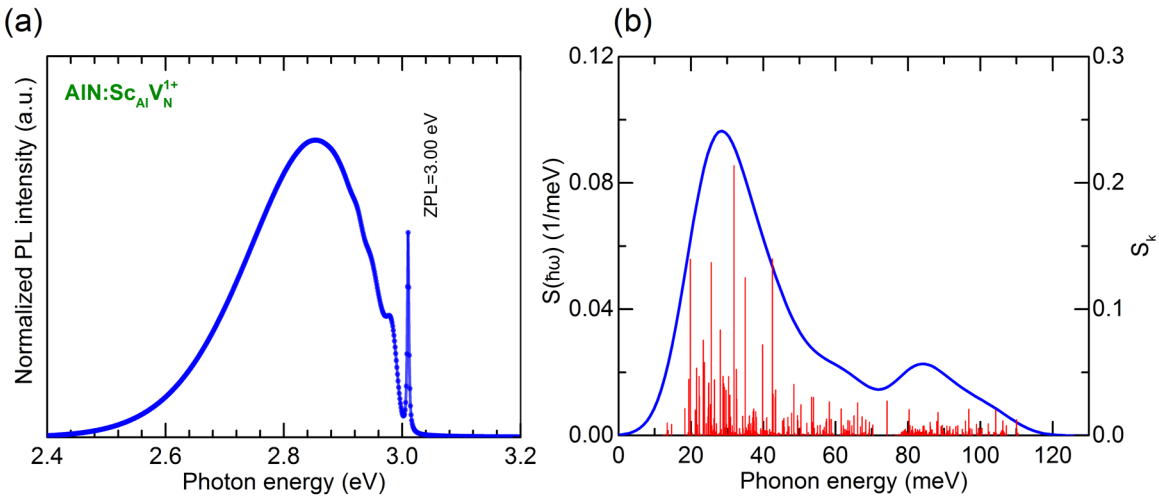

FIG. 6. (a) Calculated photoluminescence line shape associated with the $^1E \rightarrow {}^1A$ optical transition of $Sc_{Al}V_N^{1+}$. (b) Partial Huang-Rhys factor S_k and spectral function of electron-phonon coupling $S(\hbar\omega)$.

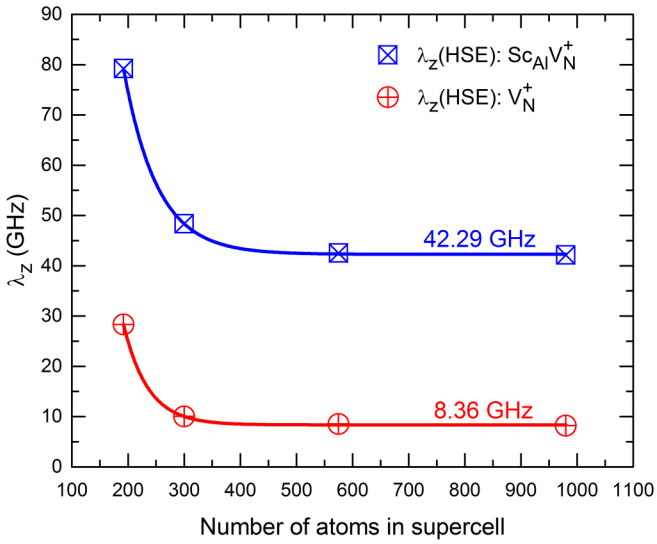

FIG. 7. Calculated axial component λ_z of SOC.

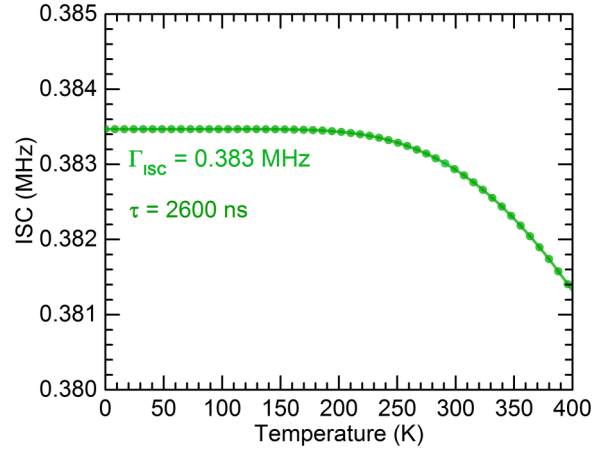

FIG. 8. Calculated intersystem crossing rate between ^1E and ^3E excited states of the $Sc_{Al}V_N^{1+}$ center as a function of temperature.

polarization protocol for qubit applications, as shown in Figs. 4 and 5. The cycle begins from the ^1A ground state, with optical pumping to the ^1E spin-conserving excited state, followed by an intersystem crossing (ISC) to the ^3E triplet shelving state.

Absorption of an $\{x, y\}$ polarized photon upon continuous illumination in the violet region of the spectrum (∼413 nm or below) places the system into the ^1E state. From the ^1E excited state, an ISC mediated by the axial λ_z component of SOC occurs selectively to the $m_s = 0$ spin projection ($E_{x,y}$).

To estimate the rate of the ISC, we calculate λ_z as described in Sec. II H. We performed this calculation for supercells of different sizes and noticed that λ_z converges faster for $(Sc_{Al}V_N)^+$ than for the NV^- center in diamond [74]. We attribute this to the larger lattice constant of AlN compared to diamond, which results in larger spatial separation of the defect wave functions and their periodic images for comparable supercell sizes. The values of λ_z as a function of supercell size are shown in Fig. 7. The converged value of λ_z for $(Sc_{Al}V_N)^+$ is 42 GHz, five times larger than for V_N^{1+}.

We then proceed to evaluate the ISC rate using Eq. (9). The calculated rate is shown in Fig. 8 and is practically independent of temperature. This is a result of the small geometry difference $\Delta Q = 0.046$ amu$^{1/2}$ Å between the ^1E and ^3E states. The calculated lifetime τ at $T = 0$ K is 2600 ns.

The ISC competes with other decay mechanisms of the ^1E excited state. For example, the rate at which the ^1E state decays radiatively by producing a photon can be calculated with

$$\Gamma_R = \frac{nE_{\mathrm{ZPL}}^3\mu^2}{3\pi\epsilon_0 c^3\hbar^4}, \tag{18}$$

where n is the reflective index of the host material, E_{ZPL} is the ZPL energy of $^1E \rightarrow {}^1A$ transition, μ^2 is the modulus square of transition dipole moment, ϵ_0 is the permittivity of free space, c is the speed of light, and $\hbar$ is the reduced Planck constant. For AlN, $n = 2.1$ at 3 eV. We calculate $\mu^2 = 19.98$ D^2, which results in $\Gamma_R = 1.86 \times 10^8$ s^{-1} and a corresponding radiative lifetime for the ^1E state of $\tau_R = 5.36$ ns. In principle, the ^1E state could also decay nonradiatively by producing phonons, however, previous work on nonradiative transitions [3] suggests that a direct nonradiative transition between the ^1E excited state and ^1A ground state will be negligibly slow for a 3-eV transition energy. We can therefore conclude that the lifetime of the ^1E excited state will be determined by the radiative process, with a finite probability of producing an ISC to the triplet state. The triplet state can therefore be initialized and read out by optical pumping, following the protocol of Ref. [31].

To be able to utilize the triplet state to manipulate a coupled nuclear spin, its lifetime must be sufficiently long. If this condition is met, the metastable triplet state can be used to transfer spin polarization onto the nuclear spin via the hyperfine interaction (see Fig. 5). Given the large energy difference from the ^1A ground state and spin-flip nature of the transition, the lifetime of the triplet state is likely set by the phosphorescence decay rate. Phosphorescence (a radiative transition involving a spin flip) is typically slow, leading to lifetimes on the order of ∼ms or longer [81], which should be sufficient to enable nuclear spin manipulation.

As demonstrated for the ST1 center in diamond [31] and the neutral carbon defect C_S^0 in WS_2 [82], optical nuclear spin polarization can be induced by the excited-state hyperfine level anticrossing while applying a small, well-tuned external magnetic field [83]. At the level anticrossing, the hyperfine interaction causes the electron spin state and the nuclear spin state to be entangled. Therefore, the spin state of the electron can be transferred to the nuclear spin, and *vice versa*. The calculated hyperfine parameters in excess of 100 MHz (see Table I) would enable efficient transfer of information between the states. After the optical pumping is turned off, the electron decays to the singlet ground state, destroying the electron spin state while leaving the nuclear spin in a polarized state. The difference in the lifetimes between individual hyperfine levels leads to different fluorescence intensities of the nuclear spin projections, providing a mechanism to read out the nuclear spin. Nuclear magnetic resonance (NMR) can be applied for coherent manipulation of a bare nuclear spin. It may be possible for $Sc_{Al}V_N$ to exhibit long spin coherence times similar to the ST1 center in diamond [31] and C_S^0 in

WS_2 [82], which is a key demand in solid-state nuclear spin quantum memories and quantum register applications.

IV. SUMMARY AND CONCLUSIONS

In summary, we analyzed the electronic structure and magneto-optical properties of V_N and $Sc_{Al}V_N$ defects in AlN with the hybrid DFT method. The positive charge state of these centers is stable across a wide range of Fermi energies. Scandium substitution on the cation site next to a nitrogen vacancy increases the localization of the defect wave functions, redshifts the emission of photons to the violet (413 nm), and enhances the ISC rate via increased SOC. We comprehensively investigated the excited-state structure of $Sc_{Al}V_N$, predicted its hyperfine parameters in the ^3E excited state, and simulated the emission line shape to facilitate further experimental analysis of the defect. Based on the resemblance of the defect's electronic structure to the ST1 center in diamond, we demonstrated the potential of $Sc_{Al}V_N$ in AlN to be used as a quantum memory in quantum information processing. This paper reports on a singlet spin-state point defect in the technologically mature w-AlN that can serve as a long-term nuclear spin quantum memory in a solid-state matrix.

ACKNOWLEDGMENTS

K.C. was financially supported by the Polish National Science Centre under Contract No. UMO-2019/32/C/ST3/00093. M.E.T. and C.G.V.d.W. were supported by the US Department of Energy, Office of Science, National Quantum Information Science Research Centers, Co-design Center for Quantum Advantage (C2QA) under Contract No. DE-SC0012704. Computing resources were provided by High Performance Computing facilities of the Interdisciplinary Centre for Mathematical and Computational Modeling (ICM) of the University of Warsaw under Grant No. GB79-16. The scientific work was carried out on the infrastructure of the Poznań Supercomputing and Networking Center. The work also used resources of the National Energy Research Scientific Computing Center, a DOE Office of Science User Facility supported by the Office of Science of the US Department of Energy under Contract No. DE-AC02-05CH11231 using NERSC Award No. BES-ERCAP0021021.

[1] J. R. Weber, W. F. Koehl, J. B. Varley, A. Janotti, B. B. Buckley, C. G. Van de Walle, and D. D. Awschalom, Quantum computing with defects, Proc. Natl. Acad. Sci. USA **107**, 8513 (2010).
[2] L. C. Bassett, A. Alkauskas, A. L. Exarhos, and K.-M. C. Fu, Quantum defects by design, Nanophotonics **8**, 1867 (2019).
[3] M. E. Turiansky, K. Parto, G. Moody, and C. G. Van de Walle, Rational design of efficient defect-based quantum emitters, APL Photonics **9**, 066117 (2024).
[4] I. Aharonovich and E. Neu, Diamond nanophotonics, Adv. Opt. Mater. **2**, 911 (2014).
[5] K. Czelej, K. Ćwieka, P. Śpiewak, and K. J. Kurzydłowski, Titanium-related color centers in diamond: A density functional theory prediction, J. Mater. Chem. C **6**, 5261 (2018).
[6] L. V. H. Rodgers, L. B. Hughes, M. Xie, P. C. Maurer, S. Kolkowitz, A. C. Bleszynski Jayich, and N. P. de Leon, Materials challenges for quantum technologies based on color centers in diamond, MRS Bull. **46**, 623 (2021).
[7] A. Gruber, A. Dräbenstedt, C. Tietz, L. Fleury, J. Wrachtrup, and C. von Borczyskowski, Scanning confocal optical microscopy and magnetic resonance on single defect centers, Science **276**, 2012 (1997).
[8] Á. Gali, *Ab initio* theory of the nitrogen-vacancy center in diamond, Nanophotonics **8**, 1907 (2019).
[9] J. P. Goss, R. Jones, S. J. Breuer, P. R. Briddon, and S. Öberg, The twelve-line 1.682 eV luminescence center in diamond and the vacancy-silicon complex, Phys. Rev. Lett. **77**, 3041 (1996).
[10] G. Thiering and A. Gali, *Ab Initio* magneto-optical spectrum of Group-IV vacancy color centers in diamond, Phys. Rev. X **8**, 021063 (2018).
[11] G. Zhang, Y. Cheng, J.-P. Chou, and A. Gali, Material platforms for defect qubits and single-photon emitters, Appl. Phys. Rev. **7**, 031308 (2020).
[12] H. Seo, M. Govoni, and G. Galli, Design of defect spins in piezoelectric aluminum nitride for solid-state hybrid quantum technologies, Sci. Rep. **6**, 20803 (2016).
[13] H. Seo, H. Ma, M. Govoni, and G. Galli, Designing defect-based qubit candidates in wide-gap binary semiconductors for solid-state quantum technologies, Phys. Rev. Mater. **1**, 075002 (2017).
[14] J. B. Varley, A. Janotti, and C. G. Van de Walle, Defects in AlN as candidates for solid-state qubits, Phys. Rev. B **93**, 161201(R) (2016).
[15] M. E. Turiansky and C. G. Van de Walle, Telecom-wavelength NV-center analogs in cubic boron nitride, Phys. Rev. B **108**, L041102 (2023).
[16] O. Madelung, *Semiconductors–Basic Data* (Springer, Berlin, 2012).
[17] C. Xiong, W. H. P. Pernice, and H. X. Tang, Low-loss, silicon integrated, aluminum nitride photonic circuits and their use for electro-optic signal processing, Nano Lett. **12**, 3562 (2012).
[18] T. Koppe, H. Hofsäss, and U. Vetter, Overview of band-edge and defect related luminescence in aluminum nitride, J. Lumin. **178**, 267 (2016).
[19] J. Y. Tsao, S. Chowdhury, M. A. Hollis, D. Jena, N. M. Johnson, K. A. Jones, R. J. Kaplar, S. Rajan, C. G. Van de Walle, E. Bellotti, C. L. Chua, R. Collazo, M. E. Coltrin, J. A. Cooper, K. R. Evans, S. Graham, T. A. Grotjohn, E. R. Heller, M. Higashiwaki, M. S. Islam *et al.*, Ultrawide-bandgap semiconductors: Research opportunities and challenges, Adv. Electron. Mater. **4**, 1600501 (2018).
[20] G. Piazza, V. Felmetsger, P. Muralt, R. H. Olsson III, and R. Ruby, Piezoelectric aluminum nitride thin films for microelectromechanical systems, MRS Bull. **37**, 1051 (2012).
[21] P. Ovartchaiyapong, K. W. Lee, B. A. Myers, and A. C. Bleszynski Jayich, Dynamic strain-mediated coupling of a single diamond spin to a mechanical resonator, Nat. Commun. **5**, 4429 (2014).

[22] A. L. Falk, P. V. Klimov, B. B. Buckley, V. Ivády, I. A. Abrikosov, G. Calusine, W. F. Koehl, A. Gali, and D. D. Awschalom, Electrically and mechanically tunable electron spins in silicon carbide color centers, Phys. Rev. Lett. **112**, 187601 (2014).

[23] A. Sedhain, L. Du, J. H. Edgar, J. Y. Lin, and H. X. Jiang, The origin of 2.78 eV emission and yellow coloration in bulk AlN substrates, Appl. Phys. Lett. **95**, 262104 (2009).

[24] T. Schulz, M. Albrecht, K. Irmscher, C. Hartmann, J. Wollweber, and R. Fornari, Ultraviolet luminescence in AlN, Phys. Status Solidi B **248**, 1513 (2011).

[25] S. Longhai, W. Nan, and X. Xuan, Strong orange luminescence from AlN whiskers, Mater. Lett. **94**, 150 (2013).

[26] M. Lamprecht, V. N. Jmerik, R. Collazo, Z. Sitar, S. V. Ivanov, and K. Thonke, Model for the deep defect-related emission bands between 1.4 and 2.4 eV in AlN, Phys. Status Solidi B **254**, 1600714 (2017).

[27] G. Liu, C. Yan, G. Zhou, J. Wen, Z. Qin, Q. Zhou, B. Li, R. Zheng, H. Wu, and Z. Sun, Broadband white-light emission from alumina nitride bulk single crystals, ACS Photonics **5**, 4009 (2018).

[28] T.-J. Lu, B. Lienhard, K.-Y. Jeong, H. Moon, A. Iranmanesh, G. Grosso, and D. Englund, Bright high-purity quantum emitters in aluminum nitride integrated photonics, ACS Photonics **7**, 2650 (2020).

[29] Y. Xue, H. Wang, N. Xie, Q. Yang, F. Xu, B. Shen, J.-j. Shi, D. Jiang, X. Dou, T. Yu, and B.-q. Sun, Single-photon emission from point defects in aluminum nitride films, J. Phys. Chem. Lett. **11**, 2689 (2020).

[30] S. G. Bishop, J. P. Hadden, F. D. Alzahrani, R. Hekmati, D. L. Huffaker, W. W. Langbein, and A. J. Bennett, Room-temperature quantum emitter in aluminum nitride, ACS Photonics **7**, 1636 (2020).

[31] S.-Y. Lee, M. Widmann, T. Rendler, M. W. Doherty, T. M. Babinec, S. Yang, M. Eyer, P. Siyushev, B. J. M. Hausmann, M. Loncar, Z. Bodrog, A. Gali, N. B. Manson, H. Fedder, and J. Wrachtrup, Readout and control of a single nuclear spin with a metastable electron spin ancilla, Nat. Nanotechnol. **8**, 487 (2013).

[32] P. Balasubramanian, M. H. Metsch, P. Reddy, L. J. Rogers, N. B. Manson, M. W. Doherty, and F. Jelezko, Discovery of ST1 centers in natural diamond, Nanophotonics **8**, 1993 (2019).

[33] S. Pezzagna, S. Diziain, H. Martelock, P. Neugebauer, J. Michaelis, T. Lühmann, and J. Meijer, Polymorphs of ^{17}O-implanted ST1 spin centers in diamond and spectroscopy of strongly coupled ^{13}C nuclear spins, ACS Photonics **11**, 1969 (2024).

[34] M. Akiyama, T. Kamohara, K. Kano, A. Teshigahara, Y. Takeuchi, and N. Kawahara, Enhancement of piezoelectric response in scandium aluminum nitride alloy thin films prepared by dual reactive cosputtering, Adv. Mater. **21**, 593 (2009).

[35] S. Fichtner, N. Wolff, F. Lofink, L. Kienle, and B. Wagner, AlScN: A III-V semiconductor based ferroelectric, J. Appl. Phys. **125**, 114103 (2019).

[36] P. E. Blöchl, Projector augmented-wave method, Phys. Rev. B **50**, 17953 (1994).

[37] G. Kresse and J. Furthmüller, Efficient iterative schemes for *ab initio* total-energy calculations using a plane-wave basis set, Phys. Rev. B **54**, 11169 (1996).

[38] G. Kresse and J. Furthmüller, Efficiency of *ab-initio* total energy calculations for metals and semiconductors using a plane-wave basis set, Comput. Mater. Sci. **6**, 15 (1996).

[39] J. Heyd, G. E. Scuseria, and M. Ernzerhof, Hybrid functionals based on a screened Coulomb potential, J. Chem. Phys. **118**, 8207 (2003).

[40] J. Heyd, G. E. Scuseria, and M. Ernzerhof, Erratum: Hybrid functionals based on a screened Coulomb potential [J. Chem. Phys. 118, 8207 (2003)], J. Chem. Phys. **124**, 219906 (2006).

[41] H. Schulz and K. Thiemann, Crystal structure refinement of AlN and GaN, Solid State Commun. **23**, 815 (1977).

[42] R. O. Jones and O. Gunnarsson, The density functional formalism, its applications and prospects, Rev. Mod. Phys. **61**, 689 (1989).

[43] T. Ziegler, A. Rauk, and E. J. Baerends, On the calculation of multiplet energies by the hartree-fock-slater method, Theor. Chim. Acta **43**, 261 (1977).

[44] U. von Barth, Local-density theory of multiplet structure, Phys. Rev. A **20**, 1693 (1979).

[45] M. Mackoit-Sinkevičienė, M. Maciaszek, C. G. Van de Walle, and A. Alkauskas, Carbon dimer defect as a source of the 4.1 eV luminescence in hexagonal boron nitride, Appl. Phys. Lett. **115**, 212101 (2019).

[46] L. Shang, Q. Chen, W. Jing, C.-G. Ma, C.-K. Duan, and J. Du, First-principles study of transition metal dopants as spin qubits, Phys. Rev. Mater. **6**, 086201 (2022).

[47] A. V. Ivanov, Y. L. A. Schmerwitz, G. Levi, and H. Jónsson, Electronic excitations of the charged nitrogen-vacancy center in diamond obtained using time-independent variational density functional calculations, SciPost Phys. **15**, 009 (2023).

[48] C. Freysoldt, B. Grabowski, T. Hickel, J. Neugebauer, G. Kresse, A. Janotti, and C. G. Van de Walle, First-principles calculations for point defects in solids, Rev. Mod. Phys. **86**, 253 (2014).

[49] C. Freysoldt, J. Neugebauer, and C. G. Van de Walle, Fully *ab initio* finite-size corrections for charged-defect supercell calculations, Phys. Rev. Lett. **102**, 016402 (2009).

[50] M. J. Rayson and P. R. Briddon, First principles method for the calculation of zero-field splitting tensors in periodic systems, Phys. Rev. B **77**, 035119 (2008).

[51] V. Ivády, I. A. Abrikosov, and A. Gali, First principles calculation of spin-related quantities for point defect qubit research, npj Comput. Mater. **4**, 76 (2018).

[52] H. Xiang, C. Lee, H.-J. Kooc, X. Gonga, and M.-H. Whangbo, Magnetic properties and energy-mapping analysis, Dalton Trans. **42**, 823 (2013).

[53] J. Li, L. Gu, and R. Wu, Slow spin relaxation in single endohedral fullerene molecules, Phys. Rev. B **104**, 224431 (2021).

[54] J. Telser, EPR Interactions: Zero-Field Splittings, in *eMagRes* (Wiley, Hoboken, NJ, 2017), pp. 207–234.

[55] M. R. Zemła, K. Czelej, and J. A. Majewski, Graphene–Iron(II) phthalocyanine hybrid systems for scalable molecular spintronics, J. Phys. Chem. C **124**, 27645 (2020).

[56] S. Mu and K. D. Belashchenko, Influence of strain and chemical substitution on the magnetic anisotropy of antiferromagnetic Cr_2O_3: An *ab-initio* study, Phys. Rev. Mater. **3**, 034405 (2019).

[57] J. P. Perdew, K. Burke, and M. Ernzerhof, Generalized gradient approximation made simple, Phys. Rev. Lett. **77**, 3865 (1996).

[58] J. P. Perdew, K. Burke, and M. Ernzerhof, Generalized gradient approximation made simple [Phys. Rev. Lett. 77, 3865 (1996)], Phys. Rev. Lett. **78**, 1396 (1997).

[59] K. Szász, T. Hornos, M. Marsman, and A. Gali, Hyperfine coupling of point defects in semiconductors by hybrid density functional calculations: The role of core spin polarization, Phys. Rev. B **88**, 075202 (2013).

[60] B. Grabowski, T. Hickel, and J. Neugebauer, *Ab Initio* study of the thermodynamic properties of nonmagnetic elementary fcc metals: exchange-correlation-related error bars and chemical trends, Phys. Rev. B **76**, 024309 (2007).

[61] J. Zhang, C.-Z. Wang, Z. Z. Zhu, and V. V. Dobrovitski, Vibrational modes and lattice distortion of a nitrogen-vacancy center in diamond from first-principles calculations, Phys. Rev. B **84**, 035211 (2011).

[62] K. Huang, A. Rhys, and N. F. Mott, Theory of light absorption and non-radiative transitions in F-centres, Proc. R. Soc. London A **204**, 406 (1950).

[63] A. Alkauskas, B. B. Buckley, D. D. Awschalom, and C. G. Van de Walle, First-principles theory of the luminescence lineshape for the triplet transition in diamond NV centres, New J. Phys. **16**, 073026 (2014).

[64] M. R. Zemła, K. Czelej, P. Kamińska, C. G. Van de Walle, and J. A. Majewski, Electronic structure and magneto-optical properties of silicon-nitrogen-vacancy complexes in diamond, Phys. Rev. B **102**, 115102 (2020).

[65] See Supplemental Material at http://link.aps.org/supplemental/10.1103/PhysRevB.110.125116 for details about the computational implementation of HR theory, formation energies for carbon and for competing defects, a visualization of the wave functions in Fig. 3(c), and which includes Refs. [64–68].

[66] M. Lax, The franck–condon principle and its application to crystal, J. Chem. Phys. **20**, 1752 (1952).

[67] R. Kubo and Y. Toyozawa, Application of the method of generating function to radiative and non-radiative transitions of a trapped electron in a crystal, Prog. Theor. Phys. **13**, 160 (1955).

[68] T. Miyakawa and D. L. Dexter, Phonon sidebands, multiphonon relaxation of excited states, and phonon-assisted energy transfer between ions in solids, Phys. Rev. B **1**, 2961 (1970).

[69] J. J. Markham, Interaction of normal modes with electron traps, Rev. Mod. Phys. **31**, 956 (1959).

[70] G. Davies, The Jahn-Teller effect and vibronic coupling at deep levels in diamond, Rep. Prog. Phys. **44**, 787 (1981).

[71] M. E. Turiansky, A. Alkauskas, M. Engel, G. Kresse, D. Wickramaratne, J.-X. Shen, C. E. Dreyer, and C. G. Van de Walle, Nonrad: Computing nonradiative capture coefficients from first principles, Comput. Phys. Commun. **267**, 108056 (2021).

[72] T. J. Smart, K. Li, J. Xu, and Y. Ping, Intersystem crossing and exciton–defect coupling of spin defects in hexagonal boron nitride, npj Comput. Mater. **7**, 59 (2021).

[73] A. M. Stoneham, *Theory of Defects in Solids: Electronic Structure of Defects in Insulators and Semiconductors*, Monographs on the Physics and Chemistry of Materials (Clarendon, Oxford, 1975).

[74] G. Thiering and A. Gali, *Ab initio* calculation of spin-orbit coupling for an NV center in diamond exhibiting dynamic Jahn-Teller effect, Phys. Rev. B **96**, 081115(R) (2017).

[75] L. Zhu, C. R. A. Catlow, Q. Hou, X. Zhang, J. Buckeridge, and A. A. Sokol, Computational study of native defects and defect migration in wurtzite AlN: an atomistic approach, J. Mater. Chem. A **11**, 15482 (2023).

[76] Q. Ren, X. Liu, Z. Ding, Y. Liu, Q. Zhou, Q. Qian, G. Zhang, H. Li, and N. Wang, Strain-controlled formation energy and migration of nitrogen vacancy in $Al_{1-x}Sc_xN$: A first-principles study, ACS Appl. Mater. Interfaces **16**, 28838 (2024).

[77] A. Janotti and C. G. Van de Walle, Native point defects in ZnO, Phys. Rev. B **76**, 165202 (2007).

[78] Q. Yan, A. Janotti, M. Scheffler, and C. G. Van de Walle, Origins of optical absorption and emission lines in AlN, Appl. Phys. Lett. **105**, 111104 (2014).

[79] J. L. Lyons, A. Janotti, and C. G. Van de Walle, Effects of carbon on the electrical and optical properties of InN, GaN, and AlN, Phys. Rev. B **89**, 035204 (2014).

[80] M. Tinkham, *Group Theory and Quantum Mechanics* (Dover, New York, 2003).

[81] G. Baryshnikov, B. Minaev, and H. Ågren, Theory and calculation of the phosphorescence phenomenon, Chem. Rev. **117**, 6500 (2017).

[82] S. Li, G. Thiering, P. Udvarhelyi, V. Ivády, and A. Gali, Carbon defect qubit in two-dimensional WS_2, Nat. Commun. **13**, 1210 (2022).

[83] V. Jacques, P. Neumann, J. Beck, M. Markham, D. Twitchen, J. Meijer, F. Kaiser, G. Balasubramanian, F. Jelezko, and J. Wrachtrup, Dynamic polarization of single nuclear spins by optical pumping of nitrogen-vacancy color centers in diamond at room temperature, Phys. Rev. Lett. **102**, 057403 (2009).